Modeling $SiH_4/O_2/Ar$ Inductively Coupled Plasmas Used for Filling of Microtrenches in Shallow Trench Isolation (STI)

Stefan Tinck,* Annemie Bogaerts

Modeling results are presented to gain a better insight in the properties of a $SiH_4/O_2/Ar$ inductively coupled plasma (ICP) and how it interacts with a silicon substrate (wafer), as applied in the microelectronics industry for the fabrication of electronic devices. The $SiH_4/O_2/$ Ar ICP is used for the filling of microtrenches with isolating material (SiO_2), as applied in shallow trench isolation (STI). In this article, a detailed reaction set that describes the plasma chemistry of $SiH_4/O_2/Ar$ discharges as well as surface processes, such as sputtering, oxidation, and deposition, is presented. Results are presented on the plasma properties during the plasma enhanced chemical vapor deposition process (PECVD) for different gas ratios, as well as on the shape of the filled trenches and the surface compositions of the deposited layers. For the operating conditions under study it is found that the most important species accounting for deposition are SiH_2, SiH_3O, SiH_3 and SiH_2O, while SiH_2^+, SiH_3^+, O_2^+ and Ar^+ are the dominant species for sputtering of the surface. By diluting the precursor gas (SiH_4) in the mixture, the deposition rate *versus* sputtering rate can be controlled for a desired trench filling process. From the calculation results it is clear that a high deposition rate will result in undesired void formation during the trench filling, while a small deposition rate will result in undesired trench bottom and mask damage by sputtering. By varying the SiH_4/O_2 ratio, the chemical composition of the deposited layer will be influenced. However, even at the highest SiH_4/O_2 ratio investigated (i.e., 3.2:1; low oxygen content), the bulk deposited layer consists mainly of SiO_2, suggesting that low-volatile silane species deposit first and subsequently become oxidized instead of being oxidized first in the plasma before deposition. Finally, it was found that the top surface of the deposited layer contained less oxygen due to preferential sputtering of O atoms, making the top layer more Si-rich. However, this effect is negligible at a SiH_4/O_2 ratio of 2:1 or lower.

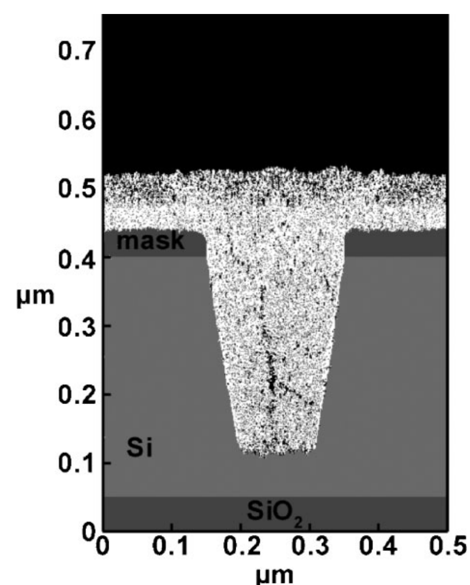

S. Tinck, A. Bogaerts
Department of Chemistry, Research Group PLASMANT, University of Antwerp, Universiteitsplein 1, B-2610 Antwerp, Belgium

S. Tinck
IMEC, Kapeldreef 75, B-3001 Leuven, Belgium
E-mail: stefan.tinck@ua.ac.be

© 2012 WILEY-VCH Verlag GmbH & Co. KGaA, Weinheim

DOI: 10.1002/ppap.201100093

1. Introduction

Plasma enhanced chemical vapor deposition (PECVD) is an appropriate process for microtrench (gap) filling during shallow trench isolation (STI) in semiconductor device processing as applied in the microelectronics industry.[1] In STI, trenches are etched in the silicon substrate, which are then filled with insulating material (SiO_2) to isolate active areas on the wafer. As microdevice nodes continue to shrink, the requirements for a decent gap filling process become increasingly challenging. To continue to meet these requirements, the PECVD process needs to be optimized and better understood. Usually high operating power and low pressure, as well as substrate bias and gas mixture, must be carefully chosen for a stable gap filling process. For mechanical and electrical stability, both structure damage and voids in the deposited layer must be avoided and therefore a well balanced operating process must be found. Both the balance between deposition rate and sputtering rate, as well as sputter deposition and ion angle, have proven to have a major effect on the resulting deposition process.[2] Sputter deposition, where the ions from the plasma are deposited into the surface layer (during sputtering of the surface), was found to be important for filling the trenches successfully.

To deposit SiO_2 in the microtrenches, typically a SiH_4/O_2 or SiH_4/N_2O mixture is applied, usually diluted with Ar, H_2 or He.[3] SiH_4 is the precursor gas, while an oxidizing agent (e.g., O_2) is added to the mixture to grow a SiO_2 film. Park and Rhee[4] have experimentally investigated the growth mechanism of low temperature SiO_2 films deposited by PECVD. The gas mixture under study in their work was SiH_4/N_2O. They concluded that SiH_2O and SiH_3O are probably the main film precursor molecules and that oxygen can remove residual −OH in the deposited layer, resulting in near stoichiometric SiO_2 films. However, gas ratios in combination with plasma power need to be chosen carefully to obtain the optimum gap fill process.[4]

The goal of this paper is to obtain more insight in the effects of different gas ratios in an $Ar/SiH_4/O_2$ gas mixture on the plasma properties and on the resulting deposition process by means of a numerical investigation. Different types of modeling work on silane plasmas used for deposition have been reported in literature. Both Kovalgin et al.[5] and Kushner[6] have numerically investigated the chemical reactions in an Ar/SiH_4 inductively coupled plasma (ICP) used for PECVD of amorphous silicon by means of an analytical and a two-dimensional (2D) hybrid model, respectively, and they presented a detailed reaction set. However, in both cases no surface reactions were included to describe the deposition processes. 2D hybrid plasma simulations on $He/SiH_4/O_2$ mixtures have also been performed by Kushner[7] who presented a detailed chemical reaction set and investigated which species are most important for deposition as a function of operating power and reactor geometry. However, also no surface reactions were included to investigate the actual deposition process. Finally, also De Bleecker et al.[8] presented a one-dimensional fluid model for He/SiH_4 mixtures containing small amounts of O_2. A detailed reaction set for the gas-phase oxidation of silane was given, but deposition and surface oxidation were again not considered in their model. On the other hand, there exist some papers in literature on modeling the oxide deposition process on a surface. Chang et al.[9] have developed a Monte Carlo profile simulator for SiO_2 deposition which includes different effects, such as angle dependent sputtering, ion-induced deposition, backscatter-deposition, and redeposition of sputtered material. Moreover, Hsiau et al.[10] have presented a feature profile model, also based on Monte Carlo simulations, that can be applied for various etching or deposition processes, including SiO_2 gap fill applications. Both papers, however, treat only the surface processes without considering the plasma.

In the present paper, a hybrid model developed by Kushner[11] is applied that is able to calculate bulk plasma properties in a 2D geometry, while taking into account also surface processes, such as sputtering and deposition at the walls. In this way, we can investigate the influence of certain process parameters such as power, pressure or gas mixture on the plasma, and, simultaneously study how a change in plasma behavior affects the resulting trench filling process.

2. Description of the Model

A hybrid Monte Carlo-fluid plasma model, i.e., the so-called hybrid plasma equipment model (HPEM), developed by Kushner,[11] is applied to describe the plasma processes and plasma–surface interactions. It consists of an electromagnetics module, where the electromagnetic fields are calculated, an electron Monte Carlo module, where the electron behavior is simulated, and a fluid part, which treats the heavy plasma species. A more detailed explanation of the model can be found in ref.[11]

This plasma model includes an extra analytical module to predict changes in the composition of the surface layers due to sputtering or deposition by plasma species. More specifically, the fluxes of all plasma species to the reactor walls and the wafer, as calculated in the plasma model, are used in this module to address the surface processes based on a surface chemistry reaction set. From here, the fluxes of surface species returning to the plasma are defined for an updated description of the plasma chemistry. The overall calculation switches between these two models in an iterative way until convergence is reached.

© 2012 WILEY-VCH Verlag GmbH & Co. KGaA, Weinheim

After convergence, an additional Monte Carlo feature profile model[12] is introduced to address microstructure changes in time (i.e., trench filling), during the PECVD process. Based on the fluxes of species arriving at the wafer, as calculated by the HPEM, this model launches Monte Carlo particles to the surface to address a change in the surface composition and trench profile as a function of time. A more detailed description of this model can be found in ref.[12]

In the following sections, we present a discussion on the different plasma species included in the model, a reaction set for the plasma reactions, and a surface chemistry reaction set.

2.1. Species Considered in the Model

Thirty-seven different plasma species are taken into account in the model, as well as nine different surface layers (also called "surface species") for addressing the wall conditions. The complete list of species is shown in Table 1.

The excited species Ar^* and O^* consist of the 4s and 4p excited levels, and 3s and 3p levels, respectively. Electron impact vibrational and rotational excitations are included for O_2, H_2 and SiH_4, but not for the other molecular reaction products. O_2 includes the ground state molecule and two electronic excited levels with thresholds of 8.40 and 10.00 eV. For each of these three states, one rotational excitation and two vibrational excitations are included with thresholds of 0.02, 0.19 and 0.38 eV. Similarly, H_2 consists of the ground state and two electronic excited states with threshold energies of 8.80 and 11.87 eV. Also two rotational and two vibrational excitations are included with threshold energies of 0.04, 0.07, 0.52 and 1.00 eV respectively. Finally, for SiH_4, two vibrational excitations are included, with thresholds of 0.11 and 0.24 eV.

Some species are not included in the model, mostly because their densities are small or because not enough information can be found on their chemical reactions. The latter is true for positive ions of SiH_xO species. No ionization cross-sections could be found for these molecules and their ions are therefore not included. Also O_2^- is not included since it is lost more rapidly by charge transfer to O^- than formed, because the threshold for the formation of O_2^- is relatively high.[13,14] Hence, we expect that the density of O_2^- in the plasma will be much lower than the O^- density, at least for these low pressure systems. Similarly, O_3 is not included in our model, because at the very low pressure under study (10 mTorr), O_3 is not likely to be abundant in the plasma.[15] The same applies for higher silane products such as Si_2H_6 or Si_nH_{2n+2} ($n > 2$). Indeed, for gap filling applications, particle formation is not desired and conditions are chosen to reduce dust formation as much as possible. Dust formation is therefore negligible at the very-low pressure and low silane gas fraction investigated here and is hence not included in the model.[6]

2.2. Plasma Chemical Reactions Included in the Model

To describe the plasma chemistry of the $SiH_4/O_2/Ar$ gas mixture, a detailed reaction set was constructed which is presented in Tables 2–6, subdivided according to the reactants, for the sake of clarity. Elastic collisions are included in the model but are not listed in the tables. The electron impact reaction rates are defined by energy

Table 1. Overview of the species included in the model.

Ground state neutrals	Ar, O_2, O, H_2, H, H_2O, OH, Si, SiH, SiH_2, SiH_3, SiH_4, $SiHO$, SiH_2O, SiH_3O, SiO, SiO_2
Positive ions	Ar^+, O_2^+, O^+, H^+, H_2^+, H_3^+, ArH^+, Si^+, SiH^+, SiH_2^+, SiH_3^+, SiH_4^+, SiO^+, SiO_2^+
Excited species	Ar^*, O^*
Negatively charged species	O^-, SiH_2^-, SiH_3^+, electrons
Surface species	$Si_{(s)}$, $SiH_{(s)}$, $SiH_{2(s)}$, $SiH_{3(s)}$, $SiO_{(s)}$, $SiO_{2(s)}$, $SiHO_{(s)}$, $SiH_2O_{(s)}$, $SiH_3O_{(s)}$

Table 2. Chemical reactions for pure Ar defined in the model.

Reaction	Cross-section or rate constant	Reference
$e + Ar \rightarrow Ar^* + e$	$\sigma(E)$	[16]
$e + Ar \rightarrow Ar^+ + 2e$	$\sigma(E)$	[16]
$e + Ar^* \rightarrow Ar^+ + 2e$	$\sigma(E)$	[16]
$e + Ar^* \rightarrow Ar + e$	$\sigma(E)$	[16]
$Ar^* + Ar^* \rightarrow Ar^+ + Ar + e$	$5.00 \times 10^{-10}\ cm^3 \cdot s^{-1}$	[16]

Plasma Process. Polym. 2012, 9, 522–539

© 2012 WILEY-VCH Verlag GmbH & Co. KGaA, Weinheim

DOI: 10.1002/ppap.201100093

Table 3. Chemical reactions for pure O_2 gas defined in the model.

Reaction	Cross-section or rate constant	Reference
$e + O_2 \rightarrow O^- + O$	$\sigma(E)$	[16]
$e + O_2 \rightarrow O + O + e$	$\sigma(E)$	[16]
$e + O_2 \rightarrow O^* + O + e$	$\sigma(E)$	[16]
$e + O_2 \rightarrow O_2^+ + 2e$	$\sigma(E)$	[16]
$e + O_2 \rightarrow O + O^+ + 2e$	$\sigma(E)$	[16]
$e + O_2^+ \rightarrow O + O$	$\sigma(E)$	[16]
$e + O^- \rightarrow O + 2e$	$1.95 \times 10^{-12}\ T_e^{-0.7} \exp[-3.4\,eV/T_e]\,cm^3 \cdot s^{-1}$	[17]
$e + O \rightarrow O^* + e$	$\sigma(E)$	[16]
$e + O \rightarrow O^+ + 2e$	$\sigma(E)$	[16]
$e + O^* \rightarrow O + e$	$\sigma(E)$	[16]
$e + O^* \rightarrow O^+ + 2e$	$\sigma(E)$	[16]
$O^- + O_2^+ \rightarrow O + O_2$	$2.00 \times 10^{-7}\ [T/298\,K]^{-0.5}\,cm^3 \cdot s^{-1}$	[18]
$O^- + O_2^+ \rightarrow O + O + O$	$1.00 \times 10^{-7}\,cm^3 \cdot s^{-1}$	[16]
$O^- + O^+ \rightarrow O + O$	$2.70 \times 10^{-7}\ [T/298\,K]^{-0.5}\,cm^3 \cdot s^{-1}$	[19]
$O^* + O \rightarrow O + O$	$8.00 \times 10^{-12}\,cm^3 \cdot s^{-1}$	[16]
$O^* + O_2 \rightarrow O + O_2$	$2.65 \times 10^{-11} \exp[67\,K/T]\,cm^3 \cdot s^{-1}$	[18]
$O^+ + O_2 \rightarrow O + O_2^+$	$2.00 \times 10^{-11}\,cm^3 \cdot s^{-1}$	[20]

Table 4. Chemical reactions for pure H_2 gas defined in the model.

Reaction	Cross-section or rate constant	Reference
$e + H_2 \rightarrow H + H + e$	$\sigma(E)$	[21]
$e + H_2 \rightarrow H_2^+ + 2e$	$\sigma(E)$	[22]
$e + H_2^+ \rightarrow H + H^+ + e$	$\sigma(E)$	[23]
$e + H_2^+ \rightarrow H + H$	$\sigma(E)$	[23]
$e + H \rightarrow H^+ + 2e$	$\sigma(E)$	[24]
$e + H_3^+ \rightarrow H^+ + H2 + e$	$\sigma(E)$	[23]
$e + H_3^+ \rightarrow H + H_2$	$\sigma(E)$	[23]
$H_2^+ + H \rightarrow H_2 + H^+$	$6.40 \times 10^{-10}\,cm^3 \cdot s^{-1}$	[6]
$H_2^+ + H_2 \rightarrow H_3^+ + H$	$2.00 \times 10^{-9}\ [T/298\,K]^{-0.5}\,cm^3 \cdot s^{-1}$	[25]

dependent cross-sections $\sigma(E)$ that can be found in the corresponding references, while the rates of the heavy particle reactions are determined by reaction rate coefficients that are directly presented in the tables. The electron collisions are electron impact ionization, dissociative ionization, excitation, and dissociation reactions, as well as electron dissociative attachment and electron–ion recombination. The heavy particle reactions include positive–negative ion recombination, charge transfer, as well as many chemical reactions to form new species, as is outlined in the tables.

2.3. Surface Reactions Included in the Model

When the plasma is in contact with a surface such as the substrate or the reactor walls, several surface processes take place. Non-volatile plasma species can deposit on the surface. Moreover, the surface is bombarded by plasma ions being accelerated through the sheath, giving rise to sputtering. In addition to deposition and sputtering, also chemical reactions can take place, such as oxidation of the surface. Table 7 presents an overview of the different surface reactions included in the model.

© 2012 WILEY-VCH Verlag GmbH & Co. KGaA, Weinheim

Table 5. Chemical reactions for pure SiH_4 gas defined in the model.

	Cross-section or rate constant	Reference
$e + SiH_4 \rightarrow SiH_3 + H + e$	$\sigma(E)$	[6]
$e + SiH_4 \rightarrow SiH_2 + H + H + e$	$\sigma(E)$	[6]
$e + SiH_4 \rightarrow SiH + H_2 + H + e$	$\sigma(E)$	[6]
$e + SiH_4 \rightarrow SiH_3^+ + H + 2e$	$\sigma(E)$	[6]
$e + SiH_4 \rightarrow SiH_2^+ + H_2 + 2e$	$\sigma(E)$	[6]
$e + SiH_4 \rightarrow SiH^+ + H + H_2 + 2e$	$\sigma(E)$	[6]
$e + SiH_4 \rightarrow Si^+ + H_2 + H_2 + 2e$	$\sigma(E)$	[6]
$e + SiH_4 \rightarrow SiH_3^+ + H$	$\sigma(E)$	[6]
$e + SiH_4 \rightarrow SiH_2^- + H + H$	$\sigma(E)$	[6]
$e + SiH^+ \rightarrow Si + H$	$1.69 \times 10^{-7}\ cm^3 \cdot s^{-1}$	[6]
$e + SiH_2^+ \rightarrow SiH + H$	$1.69 \times 10^{-7}\ cm^3 \cdot s^{-1}$	[6]
$e + SiH_3^+ \rightarrow SiH_2 + H$	$1.69 \times 10^{-7}\ cm^3 \cdot s^{-1}$	[6]
$e + SiH_3 \rightarrow SiH_3^+ + 2e$	$\sigma(E)$	[6]
$e + SiH_2 \rightarrow SiH_2^+ + 2e$	$\sigma(E)$	[6]
$SiH_4 + H \rightarrow SiH_3 + H_2$	$2.68 \times 10^{-12}\ cm^3 \cdot s^{-1}$	[6]
$SiH_4 + Si \rightarrow SiH_2 + SiH_2$	$5.33 \times 10^{-13}\ cm^3 \cdot s^{-1}$	[6]
$SiH_3 + H \rightarrow SiH_2 + H_2$	$1.00 \times 10^{-10}\ cm^3 \cdot s^{-1}$	[6]
$SiH_3 + SiH_3 \rightarrow SiH_2 + SiH_4$	$7.00 \times 10^{-12}\ cm^3 \cdot s^{-1}$	[6]
$SiH_2 + H_2 \rightarrow SiH_4$	$2.00 \times 10^{-13}\ cm^3 \cdot s^{-1}$	[6]
$SiH_2 + H \rightarrow SiH + H_2$	$7.96 \times 10^{-13}\ cm^3 \cdot s^{-1}$	[6]
$SiH_2 + H \rightarrow SiH_3$	$1.11 \times 10^{-12}\ cm^3 \cdot s^{-1}$	[6]
$SiH + H_2 \rightarrow SiH_3$	$1.98 \times 10^{-12}\ cm^3 \cdot s^{-1}$	[6]
$Si + H_2 \rightarrow SiH_2$	$6.59 \times 10^{-12}\ cm^3 \cdot s^{-1}$	[6]
$SiH_2^+ + SiH_4 \rightarrow SiH_3^+ + SiH_3$	$1.07 \times 10^{-9}\ cm^3 \cdot s^{-1}$	[6,20]
$SiH_2^+ + H_2 \rightarrow SiH_3^+ + H$	$1.01 \times 10^{-10}\ cm^3 \cdot s^{-1}$	[6]
$SiH^+ + SiH_4 \rightarrow SiH_3^+ + SiH_2$	$6.00 \times 10^{-11}\ cm^3 \cdot s^{-1}$	[6,20]
$SiH^+ + H_2 \rightarrow SiH_2^+ + H$	$1.84 \times 10^{-11}\ cm^3 \cdot s^{-1}$	[6]
$H^+ + SiH_4 \rightarrow SiH_3^+ + H_2$	$5.00 \times 10^{-10}\ cm^3 \cdot s^{-1}$	[6]
$H_2^+ + SiH_4 \rightarrow Si^+ + H_2 + H_2 + H_2$	$3.66 \times 10^{-11}\ cm^3 \cdot s^{-1}$	[6]
$H_2^+ + SiH_4 \rightarrow SiH^+ + H_2 + H_2 + H$	$3.66 \times 10^{-11}\ cm^3 \cdot s^{-1}$	[6]
$H_2^+ + SiH_4 \rightarrow SiH_2^+ + H_2 + H_2$	$6.59 \times 10^{-11}\ cm^3 \cdot s^{-1}$	[6]
$H_2^+ + SiH_4 \rightarrow SiH_3^+ + H_2 + H$	$6.23 \times 10^{-10}\ cm^3 \cdot s^{-1}$	[6]
$H_2^+ + SiH_4 \rightarrow SiH_3 + H_3^+$	$1.83 \times 10^{-11}\ cm^3 \cdot s^{-1}$	[6]
$H_3^+ + SiH_4 \rightarrow SiH_3^+ + H_2 + H_2$	$5.16 \times 10^{-10}\ cm^3 \cdot s^{-1}$	[6]
$SiH^+ + SiH_4 \rightarrow SiH_2^+ + SiH_3$	$1.95 \times 10^{-10}\ cm^3 \cdot s^{-1}$	[20]
$Si^+ + SiH_4 \rightarrow SiH_3^+ + H + Si$	$6.50 \times 10^{-10}\ cm^3 \cdot s^{-1}$	[20]
$Si^+ + SiH_4 \rightarrow SiH_2^+ + H_2 + Si$	$2.20 \times 10^{-10}\ cm^3 \cdot s^{-1}$	[20]
$Si^+ + SiH_4 \rightarrow SiH^+ + H + H_2 + Si$	$2.20 \times 10^{-10}\ cm^3 \cdot s^{-1}$	[20]
$SiH_3^+ + SiH^+ \rightarrow SiH_3 + SiH$	$5.00 \times 10^{-7}\ cm^3 \cdot s^{-1}$	[6]
$SiH_3^+ + SiH_2^+ \rightarrow SiH_3 + SiH_2$	$5.00 \times 10^{-7}\ cm^3 \cdot s^{-1}$	[6]
$SiH_3^+ + SiH_3^+ \rightarrow SiH_3 + SiH_3$	$5.00 \times 10^{-7}\ cm^3 \cdot s^{-1}$	[6]

© 2012 WILEY-VCH Verlag GmbH & Co. KGaA, Weinheim
DOI: 10.1002/ppap.201100093

Table 5. (*Continued*)

	Cross-section or rate constant	Reference
$SiH_3^+ + Si^+ \rightarrow SiH_3 + Si$	$1.00\times10^{-7}\,cm^3\cdot s^{-1}$	[6]
$SiH_3^+ + H^+ \rightarrow SiH_3 + H$	$1.00\times10^{-7}\,cm^3\cdot s^{-1}$	[6]
$SiH_3^+ + H_2^+ \rightarrow SiH_3 + H_2$	$1.00\times10^{-7}\,cm^3\cdot s^{-1}$	[6]
$SiH_3^+ + H_3^+ \rightarrow SiH_3 + H_2 + H$	$1.00\times10^{-7}\,cm^3\cdot s^{-1}$	[6]
$SiH_2^- + SiH^+ \rightarrow SiH_2 + SiH$	$5.00\times10^{-7}\,cm^3\cdot s^{-1}$	[6]
$SiH_2^- + SiH_2^+ \rightarrow SiH_2 + SiH_2$	$5.00\times10^{-7}\,cm^3\cdot s^{-1}$	[6]
$SiH_2^- + SiH_3^+ \rightarrow SiH_2 + SiH_3$	$5.00\times10^{-7}\,cm^3\cdot s^{-1}$	[6]
$SiH_2^- + Si^+ \rightarrow SiH_2 + Si$	$1.00\times10^{-7}\,cm^3\cdot s^{-1}$	[6]
$SiH_2^- + H^+ \rightarrow SiH_2 + H$	$1.00\times10^{-7}\,cm^3\cdot s^{-1}$	[6]
$SiH_2^- + H_2^+ \rightarrow SiH_2 + H_2$	$1.00\times10^{-7}\,cm^3\cdot s^{-1}$	[6]
$SiH_2^- + H_3^+ \rightarrow SiH_2 + H_2 + H$	$1.00\times10^{-7}\,cm^3\cdot s^{-1}$	[6]
$Si + SiH_4 \rightarrow SiH + SiH_3$	$3.00\times10^{-10}\,cm^3\cdot s^{-1}$	[26]
$SiH + SiH_4 \rightarrow SiH_2 + SiH_3$	$5.00\times10^{-11}\,cm^3\cdot s^{-1}$	[26]

The main process under study in this work is the filling of trenches with SiO_2. This process is mainly due to deposition of low volatile plasma species, not only SiO_y ($y = 1,2$) but also SiH_x ($x = 0$–3) and SiH_xO ($x = 1$–3), which will later become oxidized to form SiO_2 (see below). The deposition probabilities, or sticking coefficients, of these species are given in the upper part of Table 7. The less volatile a species, the higher is its sticking or deposition probability. Generally it is accepted that when more H atoms are bonded to Si, the molecule becomes more volatile. Indeed, a Si atom, or SiH, is considered to be not volatile and it will stick to the wall with a probability of 1.00[26] while SiH_4 is a gas and it will be completely reflected from the surface. SiH_2 and SiH_3 are considered to be low-volatile. Ramalingam et al.[29] and Walch et al.[30] have concluded from molecular dynamics simulations that SiH_3 can only deposit on the surface if it attaches to a dangling bond from the surface. Otherwise it will most likely abstract H from the surface, since SiH_3 has one dangling bond, and it will then be reflected as SiH_4.[32] Both Kessels et al.[26] and Agarwal et al.[33] have stated that the surface reaction probability of SiH_3 is close to 0.3 and this value was adopted in our simulations (see Table 7). SiH_2 has two dangling bonds, so it is less likely for SiH_2 to abstract two H atoms and be reflected as SiH_4. Therefore SiH_2 is considered to deposit on the surface, or if not, be reflected as SiH_2. Sriraman et al.[32] have obtained a wall loss probability of 0.4 for SiH_2 based on molecular dynamics simulations, and this value is therefore adopted in our model as the deposition probability, and no H surface abstraction reactions are included for SiH_2, in contrast to SiH_3.

It is well known that O atoms and O_2 molecules will spontaneously react with Si to form a SiO_x ($x = 1$–2) layer up to 1.3 nm in thickness. O atoms and OH molecules are considered to be reactive towards the SiH_x or SiH_xO surface ($x = 0$–3), with a reaction probability close to unity;[34] see Table 7. O_2, on the other hand, is less eager to react since it is more inert, and therefore a reaction probability of 0.01 is assumed (see Table 7). Actual etching of Si with oxygen, a process often referred to as active oxidation, happens only at high substrate temperatures (>700 K)[34–39] which is higher than the temperature considered in this work (60 °C). For this reason, no etching reactions with oxygen are considered.

Also different processes for H on the surface can occur,[40,41] such as H adsorption, H abstraction (to form H_2), etching of $SiH_{3(s)}$ (to form SiH_4),[31] diffusion into the surface layer, and insertion of H into Si–Si bonds. It is also known that H can induce crystallization of amorphous silicon by perturbation of the Si–Si bonds.[42] This has an advantage in terms of charge mobility for transistor fabrication. Of all the above processes, the abstraction of a H-atom from the surface to form H_2 through an Eley–Rideal mechanism is the most likely to occur, since it is characterized by a zero activation energy barrier.[41] Therefore, this process is included in our model, with unit reaction probability for both SiH_x and SiH_xO surface layers ($x = 1$–3); see Table 7. However, for a SiH_3 surface, the formation of volatile SiH_4 upon impact of H atoms is also included, with a reaction probability of 0.045; see Table 7. This value is adopted from Amantides et al.[31]. Incorporation of H into Si–Si bonds has a threshold energy of about 0.1 eV[33] which is much higher than the plasma gas

© 2012 WILEY-VCH Verlag GmbH & Co. KGaA, Weinheim

Table 6. Chemical reactions between Ar, O_2 and SiH_4 species defined in the model.

Reaction	Cross-section or rate constant	Reference
$Ar^+ + O_2 \rightarrow Ar + O_2^+$	$5.10 \times 10^{-11}\,cm^3 \cdot s^{-1}$	[16]
$Ar^+ + O \rightarrow Ar + O^+$	$1.00 \times 10^{-11}\,cm^3 \cdot s^{-1}$	[16]
$SiH_3^+ + Ar^+ \rightarrow SiH_3 + Ar$	$5.00 \times 10^{-7}\,cm^3 \cdot s^{-1}$	[6]
$SiH_2^- + Ar^+ \rightarrow SiH_2 + Ar$	$5.00 \times 10^{-7}\,cm^3 \cdot s^{-1}$	[6]
$SiH_3^+ + ArH^+ \rightarrow SiH_3 + Ar + H$	$5.00 \times 10^{-7}\,cm^3 \cdot s^{-1}$	[6]
$SiH_2^- + ArH^+ \rightarrow SiH_2 + Ar + H$	$5.00 \times 10^{-7}\,cm^3 \cdot s^{-1}$	[6]
$Ar^+ + SiH_4 \rightarrow Ar + Si^+ + H_2 + H_2$	$1.18 \times 10^{-11}\,cm^3 \cdot s^{-1}$	[6]
$Ar^+ + SiH_4 \rightarrow Ar + SiH^+ + H + H_2$	$4.20 \times 10^{-12}\,cm^3 \cdot s^{-1}$	[6]
$Ar^+ + SiH_4 \rightarrow Ar + SiH_2^+ + H_2$	$1.66 \times 10^{-12}\,cm^3 \cdot s^{-1}$	[6]
$Ar^+ + SiH_4 \rightarrow Ar + SiH_3^+ + H$	$2.40 \times 10^{-12}\,cm^3 \cdot s^{-1}$	[6]
$Ar^+ + H_2 \rightarrow ArH^+ + H$	$6.00 \times 10^{-10}\,cm^3 \cdot s^{-1}$	[25]
$H_2^+ + Ar \rightarrow ArH^+ + H$	$1.70 \times 10^{-9}\,cm^3 \cdot s^{-1}$	[25]
$e + ArH^+ \rightarrow Ar + H$	$1.00 \times 10^{-7}\,cm^3 \cdot s^{-1}$	[25]
$ArH^+ + H_2 \rightarrow Ar + H_3^+$	$1.50 \times 10^{-9}\,cm^3 \cdot s^{-1}$	[6,25]
$H_2^+ + Ar \rightarrow H_2 + Ar^+$	$2.20 \times 10^{-10}\,cm^3 \cdot s^{-1}$	[25]
$O + OH \rightarrow H + O_2$	$2.40 \times 10^{-11}\,cm^3 \cdot s^{-1}$	[27]
$O^* + H_2O \rightarrow OH + OH$	$2.20 \times 10^{-10}\,cm^3 \cdot s^{-1}$	[27]
$OH + H_2 \rightarrow H_2O + H$	$7.70 \times 10^{-12}\,cm^3 \cdot s^{-1}$	[27]
$OH + H \rightarrow O + H_2$	$1.48 \times 10^{-10}\,cm^3 \cdot s^{-1}$	[7,8]
$O + H_2 \rightarrow OH + H$	$3.44 \times 10^{-10}\,cm^3 \cdot s^{-1}$	[7,8]
$e + H_2O \rightarrow O^- + H_2$	$\sigma(E)$	[7]
$SiH_4 + O \rightarrow SiH_3 + OH$	$6.98 \times 10^{-12}\,cm^3 \cdot s^{-1}$	[7,8]
$SiH_4 + O^* \rightarrow SiH_3 + OH$	$3.00 \times 10^{-10}\,cm^3 \cdot s^{-1}$	[7,8]
$SiH_4 + OH \rightarrow SiH_3 + H_2O$	$1.40 \times 10^{-11} \exp[-50.3\,K/T]\,cm^3 \cdot s^{-1}$	[7,8]
$SiH_4 + O_2 \rightarrow SiH_3O + OH$	$3.00 \times 10^{-12}\,cm^3 \cdot s^{-1}$	[7,8]
$SiH_3 + O \rightarrow SiH_2O + H$	$2.16 \times 10^{-10} \exp[-1\,000\,K/T]\,cm^3 \cdot s^{-1}$	[7,8]
$SiH_3 + OH \rightarrow SiH_2O + H_2$	$8.31 \times 10^{-12}\,cm^3 \cdot s^{-1}$	[7,8]
$SiH_3 + O_2 \rightarrow SiH_2O + OH$	$6.30 \times 10^{-12}\,cm^3 \cdot s^{-1}$	[7,8]
$SiH_3 + O_2 \rightarrow SiH_3O + O$	$6.30 \times 10^{-12}\,cm^3 \cdot s^{-1}$	[7,8]
$SiH_2 + O_2 \rightarrow SiH_2O + O$	$3.75 \times 10^{-12}\,cm^3 \cdot s^{-1}$	[7,8]
$SiH_2 + O_2 \rightarrow SiHO + OH$	$3.75 \times 10^{-12}\,cm^3 \cdot s^{-1}$	[7,8]
$SiH + O_2 \rightarrow SiO + OH$	$8.50 \times 10^{-11}\,cm^3 \cdot s^{-1}$	[7,8]
$SiH + O_2 \rightarrow SiO_2 + H$	$8.50 \times 10^{-11}\,cm^3 \cdot s^{-1}$	[7,8]
$SiH_3O + O \rightarrow SiH_2O + OH$	$1.00 \times 10^{-12}\,cm^3 \cdot s^{-1}$	[7,8]
$SiH_3O + OH \rightarrow SiH_2O + H_2O$	$1.00 \times 10^{-11}\,cm^3 \cdot s^{-1}$	[7,8]
$SiH_2O + H \rightarrow SiHO + H_2$	$5.48 \times 10^{-10} \exp[-5276.4\,K/T]\,cm^3 \cdot s^{-1}$	[7,8]
$SiH_2O + O \rightarrow SiHO + OH$	$2.99 \times 10^{-11} \exp[-1547.7\,K/T]\,cm^3 \cdot s^{-1}$	[7,8]
$SiH_2O + OH \rightarrow SiHO + H_2O$	$1.25 \times 10^{-11} \exp[-85.4\,K/T]\,cm^3 \cdot s^{-1}$	[7,8]
$SiHO + H \rightarrow SiO + H_2$	$3.32 \times 10^{-10}\,cm^3 \cdot s^{-1}$	[7,8]
$SiHO + O \rightarrow SiO + OH$	$1.66 \times 10^{-10}\,cm^3 \cdot s^{-1}$	[7,8]
$SiHO + OH \rightarrow SiO + H_2O$	$1.66 \times 10^{-10}\,cm^3 \cdot s^{-1}$	[7,8]
$SiO + OH \rightarrow SiO_2 + H$	$6.65 \times 10^{-12} \exp[-2864.3\,K/T]\,cm^3 \cdot s^{-1}$	[7,8]

© 2012 WILEY-VCH Verlag GmbH & Co. KGaA, Weinheim
DOI: 10.1002/ppap.201100093

Table 6. (*Continued*)

Reaction	Cross-section or rate constant	Reference
$SiO + O_2 \rightarrow SiO_2 + O$	$2.36 \times 10^{-10} \exp[-3266.3\,K/T]\,cm^3 \cdot s^{-1}$	[7,8]
$e + SiO \rightarrow SiO^+ + 2e$	$\sigma(E)$	[28]
$e + SiO_2 \rightarrow SiO_2^+ + 2e$	$\sigma(E)$	[28]
$SiO^+ + O^- \rightarrow SiO + O$	$1.00 \times 10^{-7}\ [T/298\,K]^{0.5}\,cm^3 \cdot s^{-1}$	Based on ref.[16] a)
$SiO_2^+ + O^- \rightarrow SiO_2 + O$	$1.00 \times 10^{-7}\ [T/298\,K]^{0.5}\,cm^3 \cdot s^{-1}$	Based on ref.[16] a)

a)The reaction coefficient for this reaction is not known. Therefore, we have based the rate coefficient on that of a similar neutralization reaction as presented in ref.[16]

Table 7. Scheme of surface reactions included in the model.

Species	Probability
$Si + surface \rightarrow Si_{(s)} + surface$	1.00
$SiH + surface \rightarrow SiH_{(s)} + surface$	1.00
$SiH_2 + surface \rightarrow SiH_{2(s)} + surface$	0.40
$SiH_3 + surface \rightarrow SiH_{3(s)} + surface$	0.30 a)
$SiH_4 + surface \rightarrow SiH_4 + surface$	1.00 (reflected completely)
$SiH_xO + surface \rightarrow SiH_xO_{(s)} + surface$	1.00 ($x = 1$–3)
$SiO_y + surface \rightarrow SiO_{y(s)} + surface$	1.00 ($y = 1,2$)
$SiH_{x(s)} + O \rightarrow SiH_xO_{(s)}$ ($x = 0$–3)	1.00
$SiO_{(s)} + O \rightarrow SiO_{2(s)}$	1.00
$SiH_xO_{(s)} + O \rightarrow SiH_{x-1}O_{(s)} + H$ ($x = 1$–3)	1.00 b)
$SiH_{x(s)} + O_2 \rightarrow SiH_xO_{(s)} + O$ ($x = 0$–3)	0.01
$SiO_{(s)} + O_2 \rightarrow SiO_{2(s)} + O$	0.01
$SiH_xO_{(s)} + O_2 \rightarrow SiH_{x-1}O_{(s)} + H$ ($x = 1$–3)	0.01 b)
$SiH_{x(s)} + OH \rightarrow SiH_{x+1}O_{(s)}$ ($x = 0$–3)	1.00
$SiO_{(s)} + OH \rightarrow SiO_{2(s)} + H$	1.00
$SiH_xO_{(s)} + OH \rightarrow SiH_{x-1}O_{(s)} + H$ ($x = 1$–3)	1.00 b)
$SiH_{x(s)} + H \rightarrow SiH_{x-1(s)} + H_2$ ($x = 1$–2)	1.00
$SiH_{3(s)} + H \rightarrow SiH_{2(s)} + H_2$	0.955
$SiH_{3(s)} + H \rightarrow SiH_4$	0.045 c)
$SiH_xO_{(s)} + H \rightarrow SiH_{x-1}O_{(s)} + H_2$ ($x = 1$–3)	1.00
$SiH_{x(s)} + M^+ \rightarrow SiH_x + M$ ($x = 0$–3)	Energy-dependent sputter yield d),e)
$SiH_xO_{y(s)} + M^+ \rightarrow SiH_xO_{y-1} + M$ ($x = 0$–3) ($y = 1,2$)	Energy-dependent sputter yield d),e),f)
$SiH_{x(s)} + H^+ \rightarrow SiH_{x+1(s)}$ ($x = 0$–2)	1.00 g)
$SiH_{x(s)} + H_3^+ \rightarrow SiH_{x+1(s)} + H_2$ ($x = 0$–2)	1.00 g)

a)If SiH_3 is not deposited/incorporated in the layer, it will abstract H from the surface and be returned as SiH_4[29,30]; b)In these reactions, O or O_2 or OH diffuses into the surface layer and is therefore lost from the reaction; c)The active etching of Si in the form of SiH_4 by H atoms is discussed in more detail by Amantides et al.[31]; d)See Figure 1 for the values of the sputter yields; e)M = Ar, Si, O_2, O, SiH, SiH_2, SiH_3, SiH_4, SiO, or SiO_2; f)Oxygen is preferentially sputtered, compared to SiH_x, therefore oxygen is sputtered "first"; g)For $x = 3$, volatile SiH_4 is formed.

© 2012 WILEY-VCH Verlag GmbH & Co. KGaA, Weinheim

temperature in our work or the surface temperature (60 °C), so this process will not likely occur for neutral H, but it can happen for H^+ and H_3^+ ions since they are accelerated through the sheath. H_2^+ is less likely to incorporate H compared to H^+ and H_3^+, because it is more likely to simply be neutralized at the surface and reflected as H_2. For this reason no chemical reactions for H_2^+ and H_2 are included in the surface reaction scheme.

Besides deposition reactions, the surface is also sputtered by ions. When an ion with energy of a few 100 eV arrives at the substrate, it will penetrate into the surface and cause a collision cascade, which might result in launching one or more surface atoms into the gas phase, called sputtering. Matsunami et al.[43] have proposed a formula based on experimental data to predict the sputter yield (SY) of various monoatomic ions on various surfaces. The SY for Ar^+, Si^+, O^+ and H^+ on poly-Si, implemented in our model, are based on this formula and are plotted as a function of bombarding energy in Figure 1. For ions such as SiO_2^+, these data are often not available, but we can consider the molecular ion as a sum of separate atoms arriving at the surface. Indeed, it is known that the ion will attract an electron from the surface (Auger electron) and be neutralized before collision with the surface. In this neutralization process, the molecule often dissociates. As a result, atomic fast neutrals are the actual species that arrive at the surface. Of course, the sum of the energies of the dissociated "parts" (or atoms) must be equal to the total energy of the original molecular ion.

For example, when a SiO_2^+ ion arrives at the surface with energy of 600 eV, we can assume that this ion is neutralized and dissociates, and it is actually Si + 2 O atoms arriving at the wafer with a total energy of 600 eV. Please note that in the simulation it is still SiO_2^+ bombarding the wafer, so one

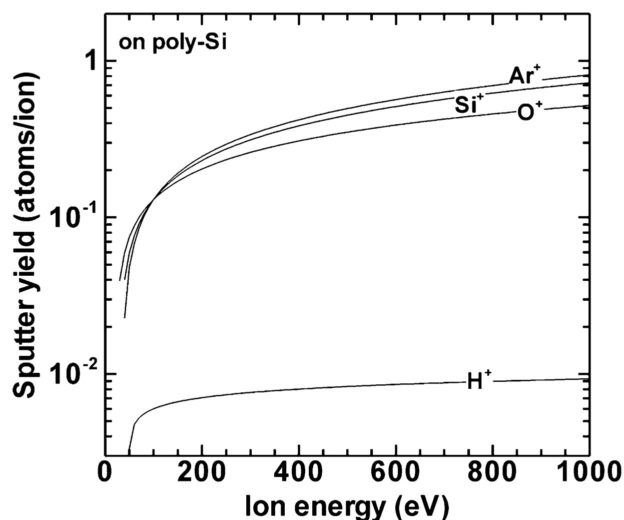

Figure 1. Energy dependent sputter yields for the monoatomic ions included in the model, adopted from ref.[43]

positive charge is arriving. Dividing the energy over the separate atoms is done based on their masses. Hence, 47% of the energy will be transferred to Si and 26.5% to each of the O atoms. Or in other words, Si will arrive with energy of 280 eV, and both O atoms with 160 eV each. This leaves us with the final equation:

$$SY[SiO_2^+](600\,eV) = SY[Si](280\,eV) + 2 \times SY[O](160\,eV)$$

Since the energy dependent SY of Si and O are known from experimental data, we can calculate and implement a SY for SiO_2^+ and all other molecular ions based on this equation, which is a possible solution when the SY for a particular ion is not experimentally available.

It should be noted that the SY presented in Figure 1 are valid for ions arriving perpendicular to the surface, which is true for most ions when they are accelerated through the sheath. To account for an angle dependent SY, which is important for trench sidewall sputtering, the SY are multiplied by an angular factor that gives rise to an optimal SY at around 60 degrees from the normal of the surface, as is known from classical sputtering theory.[44]

Besides sputtering, some ions can also react chemically with the surface atoms. For example, O^+ can penetrate the top surface layers of the substrate and cause a Si atom to be sputtered. The O atom (i.e., neutralized O^+ ion) can then be reflected or it can reside on the surface or inside the top surface layers, where it will probably react with another Si atom to form SiO. This probability is assumed to be the same as for the neutral O atoms, as presented in Table 7. In this way, ion deposition is also included in our model.

In practice, the surface will have a SiH_xO_y composition close to SiO_2, as will be illustrated below. Indeed, since SiH_x species are more volatile than pure Si, we consider them to be sputtered more easily. We could not find reliable data for the SY of SiH_x layers; therefore, we assumed values based on yields proposed by Hoekstra et al.[12] for sputtering $SiCl_x$ layers under similar operating conditions.

When a SiO_2 layer is sputtered, the O atoms will be removed at a higher rate than Si, yielding a Si-rich surface layer. This process is known as preferential sputtering.[45–49] It has indeed been reported that oxygen is sputtered about five times faster than silicon,[45] making the top surface layer of about 9 nm to consist of practically pure silicon.[46] Therefore, the SY for oxygen in SiO_2 was defined as being five times that of Si in our model, and we have considered reactions where only oxygen is removed from SiO_2 until the layer consists of pure Si. Subsequently, from then on, the SY is the same as for clean Si (cf. Figure 1). In practice, this results in a sputter rate for SiO_2 which is about half that for pure Si. This corresponds indeed to experimental observations, where SiO_2 is found to be sputtered more slowly than poly-Si. Mizutani[48] indeed observed, for an ion energy range of 400–700 eV, that a

© 2012 WILEY-VCH Verlag GmbH & Co. KGaA, Weinheim
DOI: 10.1002/ppap.201100093

clean Si layer is sputtered roughly twice as fast as a SiO_2 layer under the same conditions.

Finally, note that sputtering by H^+, H_2^+ and H_3^+ is negligible compared to the other ions due to their low mass and therefore poor energy transfer. However, incorporation of H into Si–Si bonds is likely to happen by these ions (see last two reactions in Table 7).

3. Results and Discussion

Simulations are performed for a reactor geometry of an ICP used for gap filling applications as applied in STI.[1] The 2D geometry is presented in Figure 2. When rotating this plane around the left axis the full cylindrical reactor is obtained. The reactor has two coils, i.e., a planar coil on top of the chamber and a cylindrical coil surrounding the chamber. At the bottom of the chamber the silicon substrate is located, which is a 300 mm wafer placed on top of the substrate electrode that attracts the ions from the plasma. Calculations are performed for the following operating conditions typically used for gap filling in STI: 13.56 MHz operating frequency applied both at the substrate and the coil, 10 mTorr total gas pressure, 4 400 W total coil power where 1 300 W comes from the top coil, 3 500 W substrate bias power, 60 °C wall and substrate temperature, 500 sccm total gas flow rate. The gas consists of 16% Ar, 30% SiH_4 and 54% O_2. This gas ratio will be varied as explained in more detail in the following sections.

For these conditions, the effects on the plasma characteristics of power deposition and other process parameters such as nozzle position have already been theoretically investigated by Kushner[7] for almost similar gas mixtures (with He instead of Ar). In our work, the influence of different gas mixtures on both the plasma and deposition process is investigated. We found that a gas mixture of 16% Ar, 30% SiH_4 and 54% O_2 gives rise to proper gap filling conditions, as will be demonstrated below. Hence, before focusing on the effect of the different gas ratios on the gap filling process, we will first present in Figure 3a–f several plasma properties under these conditions, to illustrate the general plasma characteristics in our ICP reactor.

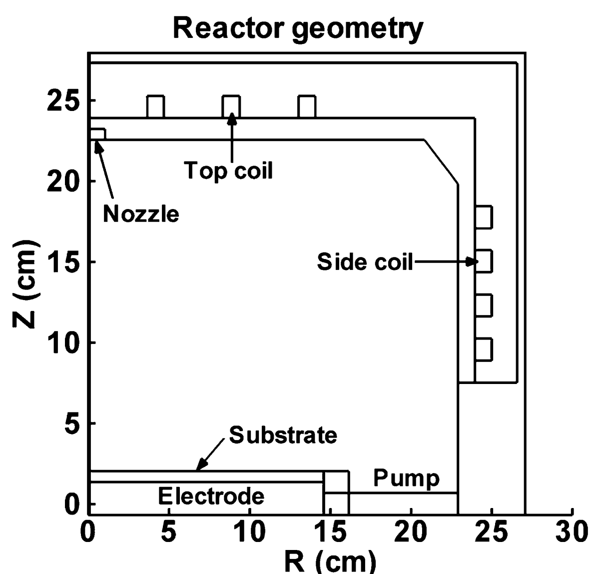

Figure 2. Two-dimensional reactor geometry defined in the model. The left axis is the symmetry axis of the cylindrically symmetrical reactor.

The electron temperature is illustrated in Figure 3a with a maximum near the top and side coils, resembling the shape of the power deposited from these coils. The maximum electron temperature is about 4 eV. Figure 3b shows the gas temperature. The gas is injected in the chamber at room temperature (293 K) and is heated slightly above 400 K in the reactor chamber. The electron density (Figure 3c) has a torodial shaped maximum which is a direct consequence of the power deposition of both top and side coils. The maximum density is slightly shifted to the center of the chamber, compared to the power deposition and maximum electron temperature (cf Figure 3a), due to the fact that electrons are lost rapidly to the walls at this low pressure. The rapid loss of electrons to the walls is also the reason why the plasma potential has a rather high positive value of about 100 V. Indeed, due to the high power from coils and substrate bias, the electrons are strongly accelerated and they can escape from the bulk plasma relatively easily due to the rather long mean free path (close to 1 cm at 10 mTorr). Finally, Figure 3e and f shows the density profiles of SiH_2 and of the sum of all ions, respectively. SiH_2, together with SiH_3O, is the most important precursor for the gap filling process, as will be illustrated below. Its density is highest in the centre of the reactor since SiH_2 is lost at the walls by deposition. The same is true for the profile of the ions that are neutralized at the reactor walls. Density profiles of most plasma species have similar shapes and are quite uniform above the wafer which is desired for a uniform deposition process. In the following sections, the effects of Ar and O_2 gas fraction will be discussed.

3.1. Effects of Ar Gas Fraction

As mentioned before, we found that the above mentioned operating conditions, more specifically a gas mixture of 16% Ar, 30% SiH_4, and 54% O_2, yielded a successfull trench filling. To illustrate this, and to understand better why this specific gas mixture is optimal, we will vary here the fraction of Ar while keeping a constant SiH_4/O_2 ratio of 1:2. Indeed, SiH_4 is considered the precursor for filling the trenches, while oxygen will convert the SiH_x species into SiO_2, which is the desired isolating material for gap filling. The Ar fraction was varied from 5 to 90% and the reactor averaged plasma

© 2012 WILEY-VCH Verlag GmbH & Co. KGaA, Weinheim

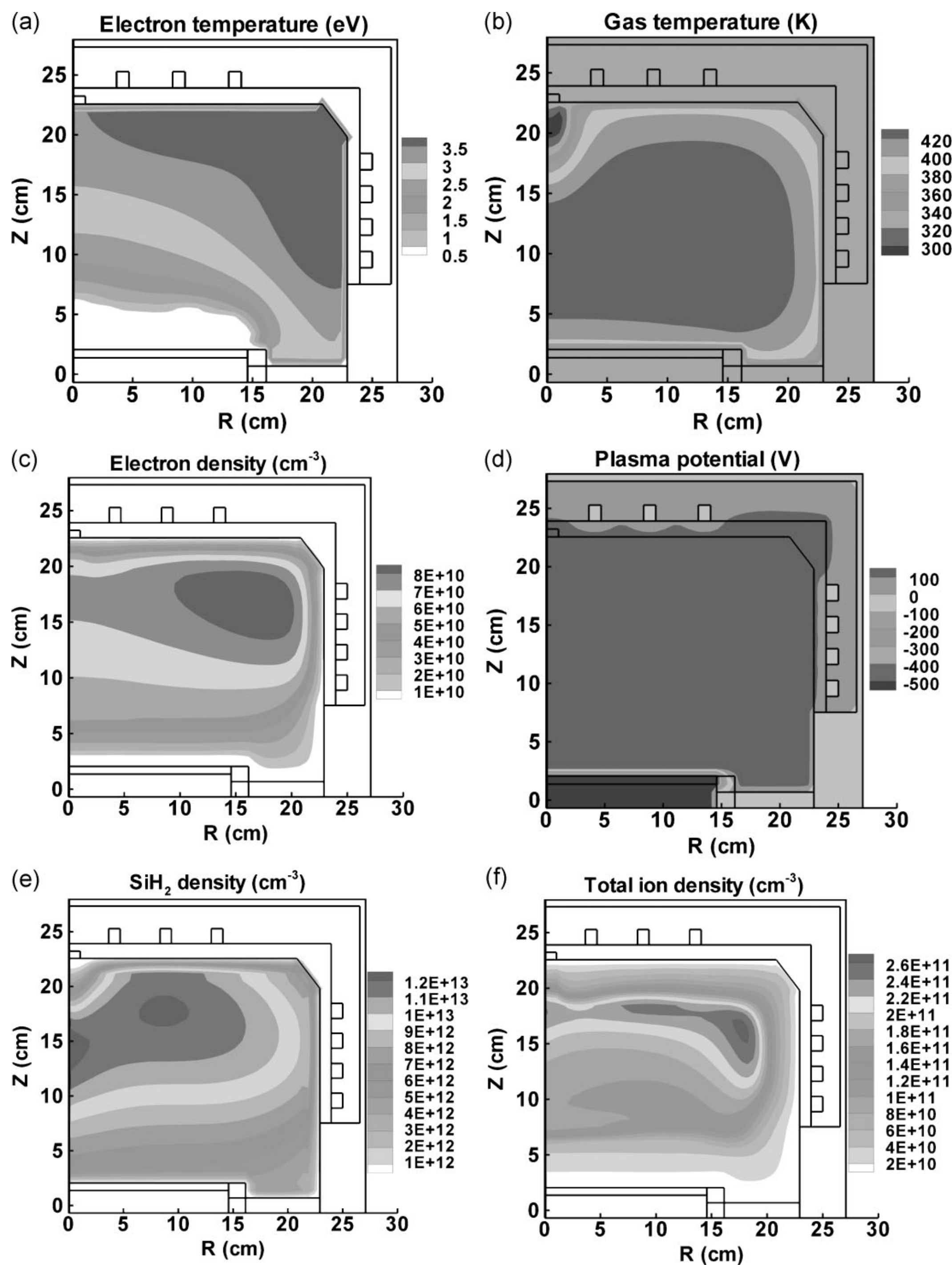

Figure 3. 2D contour plots of (a) electron temperature, (b) gas temperature, (c) electron density, (d) plasma potential, (e) SiH_2 density, and (f) total ion density. The operating conditions are: 13.56 MHz applied at coil and substrate electrode, 10 mTorr total gas pressure, 4 400 W total coil power, 3 500 W substrate bias power, 60 °C wall and substrate temperature, 500 sccm gas flow rate, and a gas mixture of 16% Ar, 30% SiH_4 and 54% O_2.

species densities are presented in Figure 4a–d. The densities of all plasma species included in the model are shown except for Ar^* and O^*, since they were found to be negligible compared to the densities of their ground state counterparts. For clarity, the results are subdivided in four plots showing (a) the neutral Si-containing species, (b) the remaining neutral species, (c) Si-containing ions, and (d) remaining ions and electrons.

Plasma Process. Polym. **2012**, *9*, 522–539
© 2012 WILEY-VCH Verlag GmbH & Co. KGaA, Weinheim
DOI: 10.1002/ppap.201100093

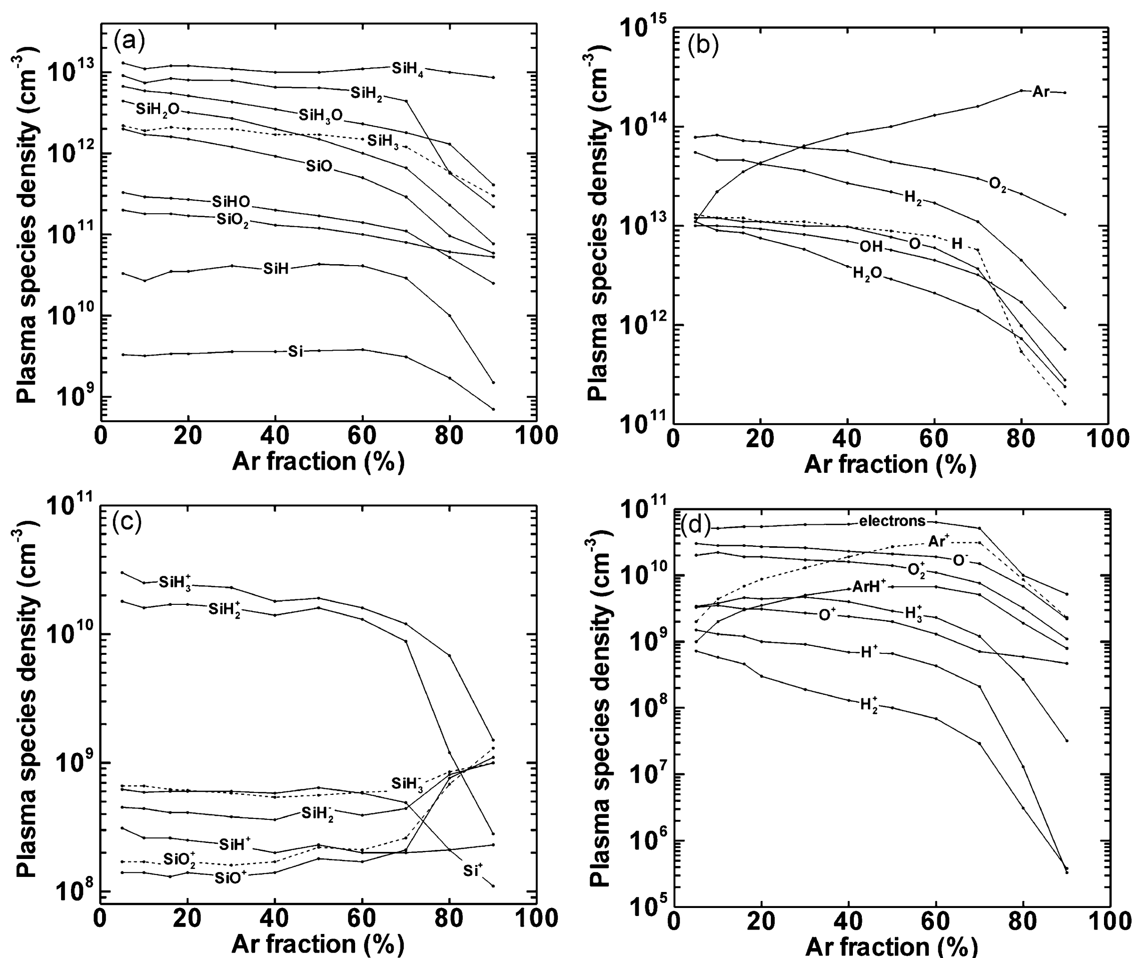

Figure 4. Reactor averaged species densities as a function of Ar gas fraction, divided over four plots for clarity: (a) neutral Si-containing species, (b) other neutral species, (c) Si-containing ions, and (d) remaining ions and electrons. The other operating conditions are the same as in Figure 3, and the ratio between SiH_4 and O_2 was kept constant at 1:2. Some lines are dashed for clarity.

From Figure 4 it can be concluded that Ar, O_2 and H_2 are the most abundant species in the plasma. Apart from Ar, all other neutral species densities decrease at higher Ar gas fraction as expected. Although SiH_4 is the most abundant Si-containing species, it is consumed for more than 60%. It should be realized that SiH_4 does not account for deposition since it is volatile (see Table 7), so the most important species for deposition are therefore SiH_2, SiH_3O, SiH_3, and SiH_2O. SiO, SiHO and SiO_2 have lower densities and fluxes to the substrate and are less important for the deposition process. This is certainly true for SiH and Si, which have very low densities, in spite of the fact that they have a sticking probability of 1. O and OH, which are present at high densities, will oxidize the surface, but they will not account for deposition as they do not contain Si. Finally, the H atoms have a flux close to that of O, and are important for abstracting H from the surface, facilitating chemical conversion of SiH_x to SiO_2.

Figure 4c and d illustrates the densities of the various ions as a function of Ar fraction. The total ion density is not presented, but it exhibits a similar trend as the electron density, depicted in Figure 4d. The total ion density is largely dependent on the total power deposition and varies therefore only slightly as expected. However, it tends to decrease at very high Ar fraction (80–90%). The reason for this is explained as follows. SiH_4 is ionized more easily than Ar because it has a lower ionization threshold (12.20 eV to form SiH_3^+ and 13.50 eV to form SiH_2^+, compared to 15.76 eV to form Ar^+). Therefore, a higher Ar fraction, or a lower fraction of silane, will result in less total ionization and a lower total ion density. On the other hand, when the Ar fraction increases, the mixture tends to change from a molecular plasma to an atomic plasma. Since atoms can not be rotationally or vibrationally excited, the electrons have more energy for ionization processes in an atomic gas mixture. Both effects seem to result in a practically constant

© 2012 WILEY-VCH Verlag GmbH & Co. KGaA, Weinheim

total ion density when the Ar fraction is varied. Only at >80% Ar the first effect seems to dominate and eventually results in a decrease of the total ion density. The densities of Ar^+ and ArH^+ first increase with Ar gas fraction and then decrease at even higher Ar fraction (Figure 4d) for a similar reason.

The most important ions that will account for sputtering of the substrate are SiH_3^+, SiH_2^+ and O_2^+ at low Ar fraction, but at an Ar fraction above 40%, Ar^+ and ArH^+ become more important as expected (Figure 4c and d).

Some other less important Si-containing ions (i.e., SiH_2^-, SiH_3^-, SiO^+ and SiO_2^+) increase in density when the silane fraction is reduced, which might be unexpected at first sight (Figure 4c). The most important losses for these ions are neutralization with ions of opposite charge. SiH_2^- and SiH_3^- are lost mostly through neutralization with H^+ and H_2^+, whose densities decrease faster than those of the Si-containing species at higher Ar gas fraction, as can be seen in Figure 4d. Similarly, SiO^+ and SiO_2^+ are lost due to neutralization with O^-, the most abundant negative ion, which also decreases in density at higher Ar percentage.

The resulting gap filling process is dependent on two major effects, namely the deposition rate of low-volatile Si-containing species and the sputtering by ions. By varying the Ar gas fraction, we can clearly see a different contribution from both effects. Figure 5 shows the total flux of species that account for deposition, together with the total flux of ions accounting for sputtering, both on the left axis. On the right axis, the resulting deposition rate is plotted, which is a result from the analytical surface model. As mentioned before, the most important species that account for deposition are SiH_2, SiH_3O, SiH_3, and SiH_2O. Their relative contributions to the total flux resemble

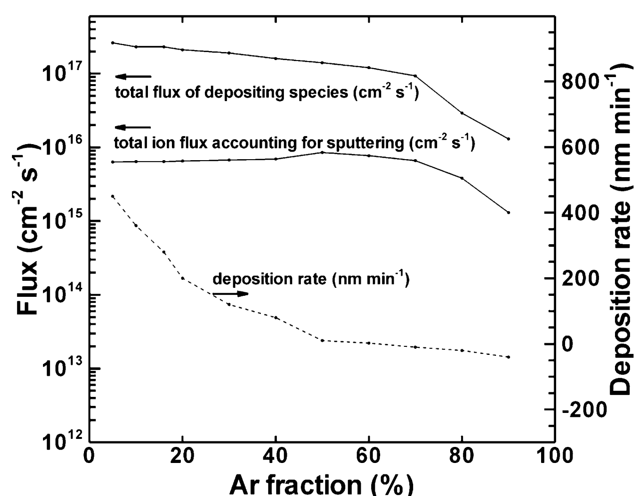

Figure 5. Total flux of all species that account for deposition (left axis), and of all ions that account for sputtering (left axis), as well as calculated deposition rate (right axis) as a function of Ar gas fraction.

those for the reactor averaged densities as presented in Figure 4a. The same is true for the contributions of the total ion flux where SiH_3^+, SiH_2^+ and O_2^+ at low Ar fraction, and Ar^+ at an Ar fraction above 40%, are the most important ions for sputtering (Figure 4c and d). As is clear from Figure 5, the depositing flux decreases with increasing Ar fraction as expected, while the ion flux is practically constant, except at higher Ar fraction. As a result, the ratio between deposition and sputtering decreases at higher Ar fraction. For example, at 10% Ar, the deposition flux is about 35 times higher than the ion flux, while at 90% Ar, this ratio is close to 10. It should be noted that not all species will deposit since the probability for sticking/deposition is not always 1 for all species. In addition, the ions have high energy (close to 600 eV) so that more than one surface atom/molecule can be sputtered per ion. It is clear from Figure 5 that this balance between deposition and sputtering has a profound effect on the resulting deposition rate, which decreases more or less linearly with Ar fraction. At a low Ar fraction of 5%, the deposition rate is around 400–500 $nm \cdot min^{-1}$, while at an Ar fraction of 60% the deposition rate has dropped to a value close to 0. Indeed, more sputtering will occur instead of deposition (=negative value for deposition rate).

It should be noted that the deposition rate is calculated in the analytical surface model, which does not take micro-trench structures into account. It treats the surfaces of the substrate and the reactor walls as a one-dimensional line in the 2D geometry, so that only the upper layer surface properties are calculated. The deposition rate is simply predicted by counting the number of deposition reactions while substracting the number of sputter reactions. More detailed results on the deposition process in the trenches can be seen in Figure 6a–c which illustrates calculation results obtained with the microscale Monte Carlo feature profile model.

At low Ar percentage (5%, Figure 6a), the deposition flux is very high, resulting in dominant deposition over sputtering, as was also shown in Figure 5. This results in serious void formation. Hence, the deposited layer is not appropriate for device fabrication due to a lack of electronic and mechanical stability. Indeed, during wafer processing, the wafer is heated and cooled down on various occasions, increasing the risk of structure damage if voids are present in the layer. At 16% Ar (Figure 6b), the deposition rate is slightly lower, but void formation is inhibited as desired. Finally at higher Ar fraction (>60%; Figure 6c), there is a strong competition between sputtering of the layer and deposition, resulting in deposition on the sidewalls, but also in damaging the device at the bottom and the mask, which must be avoided of course.

The chemical composition of the deposited layer was calculated in the analytical surface model and was found to be $SiH_{0,5}O_{1,14}$. This chemical composition was predicted for all investigated Ar gas fractions (ranging from 5 to 90%). It

© 2012 WILEY-VCH Verlag GmbH & Co. KGaA, Weinheim
DOI: 10.1002/ppap.201100093

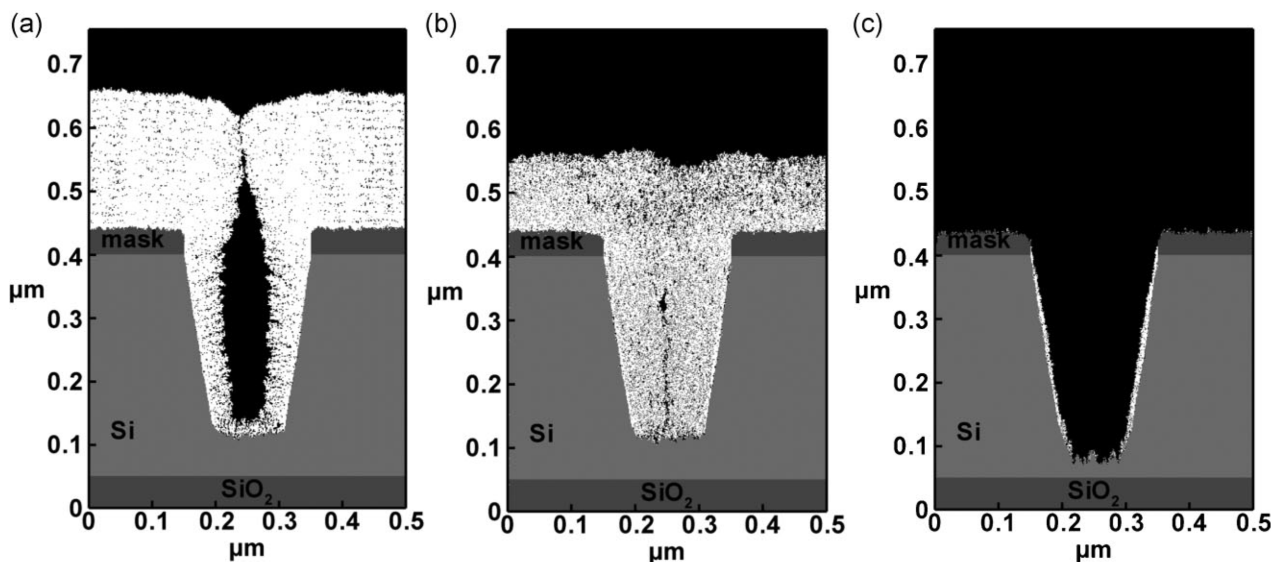

Figure 6. (a) Calculated deposition profiles at (a) 5% Ar, where a void is formed, (b) 16% Ar where a proper gap filling process takes place, and (c) 80% Ar, where trench damage occurs.

should be noted, however, that in the analytical surface model only the properties of the top surface monolayer are calculated. As mentioned before, the SiO_2 layer becomes Si-rich at the surface due to preferential sputtering of oxygen. This is why a rather low ratio of 1:1.14 is predicted for Si:O in the chemical composition of the top surface layer. In the underlying layers, the composition is closer to SiO_2, as can be concluded from Figure 6 where the deposited layer (white) has a near-SiO_2 composition.

From these results it can be concluded that the shape of the deposited layer inside the trenches can be controlled by varying the ratio between deposition and sputtering. This, in turn, can be achieved by varying the fractions of Ar and precursor gas (SiH_4) in the gas mixture. We found that an Ar gas fraction close to 16% yields optimal conditions for proper gap filling. This value is indeed found back in typical gap filling recipes in the STI process.[50]

Finally, it should be realized that in the plasma, not a very large fraction of the silane species is oxidized, as was clear from Figure 4, while the deposited layer is close to SiO_2. This indicates that mostly silane species with high hydrogen content, such as SiH_2 and SiH_3, deposit and that they are subsequently oxidized on the surface (to SiO_2) rather than in the plasma. This is schematically illustrated in Figure 7.

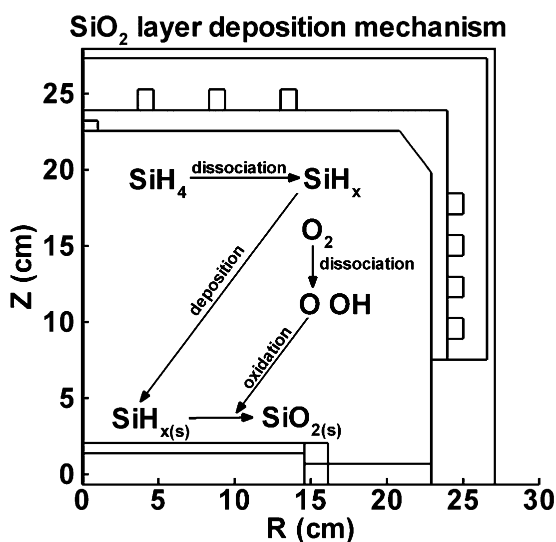

Figure 7. Schematic illustration of the mechanism for deposition of a SiO_2 layer from an Ar/SiH_4/O_2 plasma.

3.2. Effects of SiH_4/O_2 Ratio

The plasma characteristics and deposition process were also numerically investigated while varying the SiH_4/O_2 ratio. As mentioned before, we found that the trenches are filled successfully with SiO_2 when applying a gas mixture of 16% Ar, 30% SiH_4 and 54% O_2. To understand why this specific SiH_4/O_2 ratio gives rise to successful gap filling, we have varied the oxygen fraction between 20 and 80%, while keeping the Ar fraction constant at 16% The plasma species densities are presented in Figure 8a–d as a function of O_2 gas fraction. The densities are again subdivided into four plots for the sake of clarity. Figure 8a shows densities of the neutral Si-containing species, Figure 8b of the remaining neutrals, Figure 8c of the Si-containing ions, and Figure 8d of the remaining ions and free electrons. The Ar^* and O^* densities are not plotted due to their low values compared to the densities of their ground state equivalents.

© 2012 WILEY-VCH Verlag GmbH & Co. KGaA, Weinheim

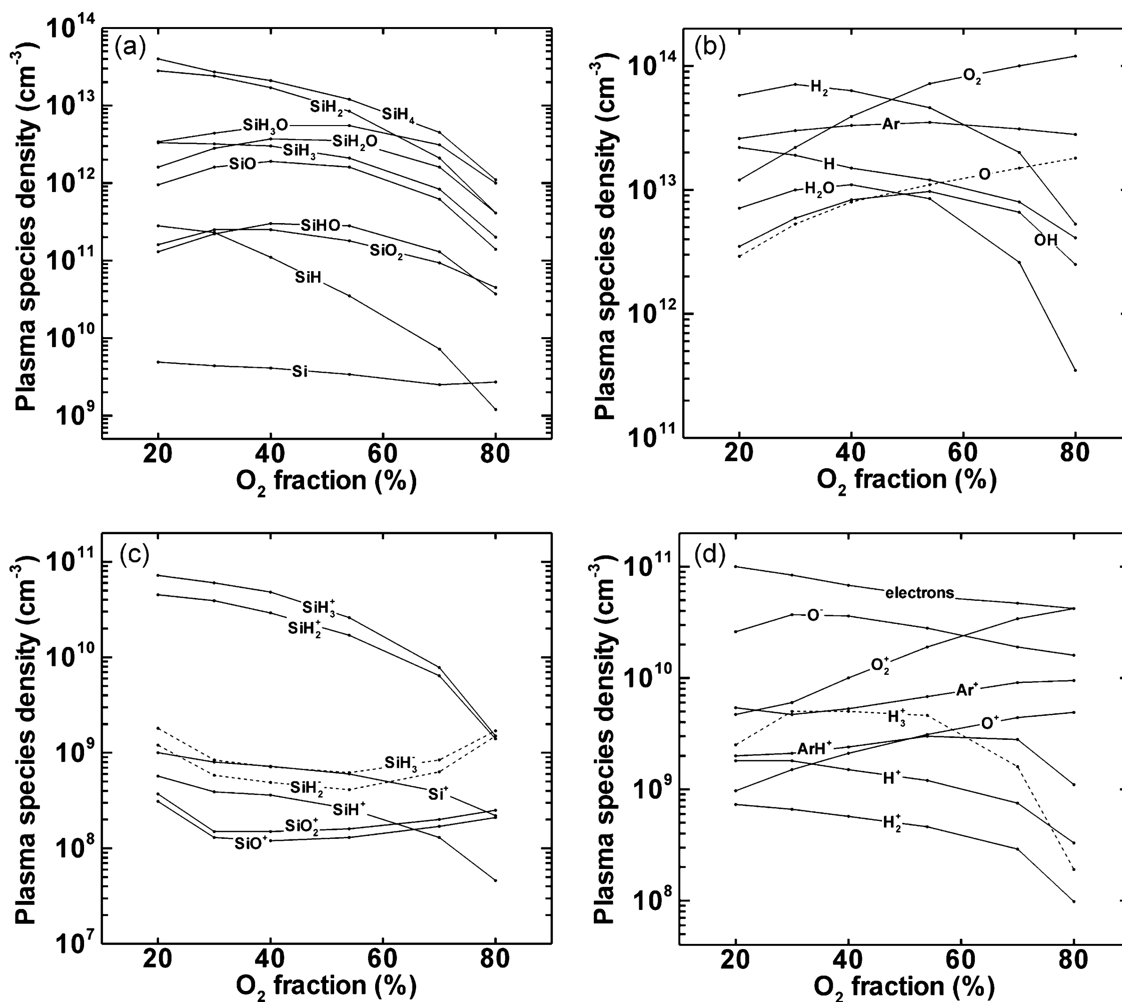

Figure 8. Reactor averaged species densities as a function of O_2 gas fraction, while the Ar fraction was kept constant at 16%, divided over four plots for clarity: (a) neutral Si-containing species, (b) other neutral species, (c) Si-containing ions, and (d) remaining ions and electrons. The other operating conditions are the same as in Figure 3.

The neutral species densities change as a function of O_2 fraction as expected (Figure 8a and b). Indeed, when the fraction of O_2 is increased, the densities of all Si-containing species decrease, while the reaction products between oxygen and silane (i.e., SiHO, SiH_2O, SiH_3O, SiO and SiO_2) tend to show maxima at intermediate fractions of O_2 and SiH_4. Moreover, the Si-containing ions all decrease in density upon increasing oxygen fraction, except SiH_2^-, SiH_3^-, SiO^+ and SiO_2^+ which exhibit local minima at a certain O_2 fraction, for the same reasons as described in Section 3.1 when the Ar fraction was varied. At higher O_2 fraction and lower silane fraction, less ions are generated and the total ion density (and electron density) decreases slightly, as also discussed in Section 3.1.

Both the amounts of precursor gas (SiH_4) and oxidizing agent (O_2) change as a function of O_2 gas fraction, so we can expect a variation in deposition rate, as well as in chemical composition of the deposited layer. Figure 9 shows the total flux of depositing species (SiH_3, SiH_2, SiH, Si, SiHO, SiH_2O, SiH_3O, SiO and SiO_2), the total ion flux and the fluxes of the oxidizing species (O_2, O and OH) on the left axis, as well as the resulting deposition rate on the right axis, as a function of O_2 percentage. Similar to the case where the Ar fraction was varied (Figure 5), the flux of depositing species is almost 40 times higher than the ion flux at the lowest O_2 fraction (and highest silane content) investigated, whereas it is only one order of magnitude higher at 80% O_2 (and 4% of SiH_4). This results in a decrease of the deposition rate at increasing O_2 fraction as expected.

Similar conclusions can be drawn for the shape of the deposited layer in the trench as shown in Figure 10a–c. If the deposition rate is close to 500 nm · min^{-1}, at a fraction of 40% O_2 or lower, deposition is dominant and a void is created (see Figure 10a). As mentioned earlier, a successfull

© 2012 WILEY-VCH Verlag GmbH & Co. KGaA, Weinheim
DOI: 10.1002/ppap.201100093

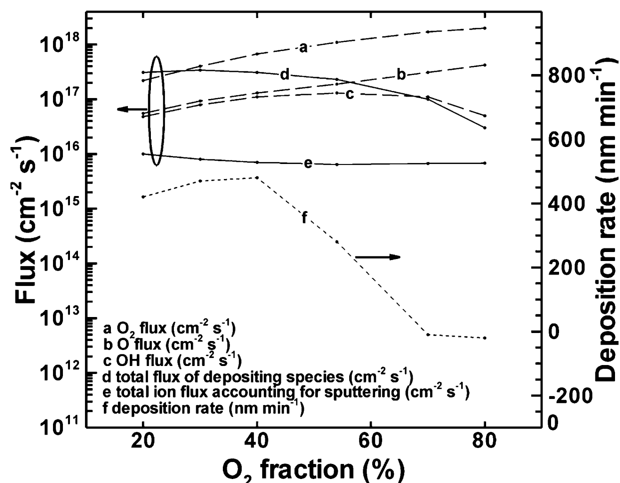

Figure 9. (Left axis) wafer averaged flux of (a) O_2, (b) O, (c) OH, (d) all species that account for deposition, and (e) all ions that account for sputtering, as a function of O_2 gas fraction. (Right axis) calculated deposition rate as a function of O_2 gas fraction.

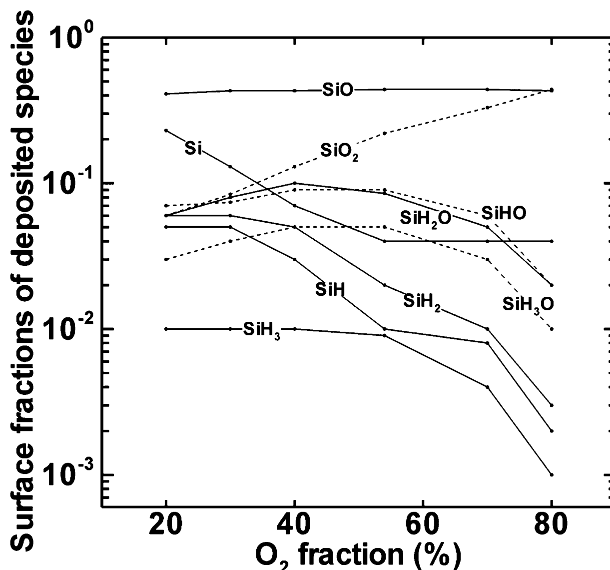

Figure 11. Calculated surface fractions of deposited species, or in other words, chemical composition of the top surface layer of the deposited layer in the trench as a function of O_2 content in the gas mixture.

filling process occurs at 54% O_2 (see Figure 10b, which corresponds in fact to the same conditions as given in Figure 6b). At very low deposition rate, (>60% of O_2) the mask and bottom of the trench are damaged, as is clear from Figure 10c.

It is interesting to note that the deposition rate increases from 20 to 40% O_2 even when the precursor gas fraction is decreased. Indeed, at low oxygen fraction, the species that accounts most for deposition is SiH_2, which does not deposit with a probability of unity (Table 7). If more oxygen is present, SiH_xO ($x = 1–3$) species become more important for deposition, and they are characterized by a deposition probability equal to 1 (see Table 7), and this explains the increase in the total deposition rate.

Naturally, the fluxes of the oxidizing agents increase with O_2 fraction, so we can expect an increase in oxygen content in the chemical composition of the deposited layer. The chemical composition of the top surface layer, or more specifically, the surface fraction of deposited species in this layer, is plotted in Figure 11 as a function of O_2 gas fraction.

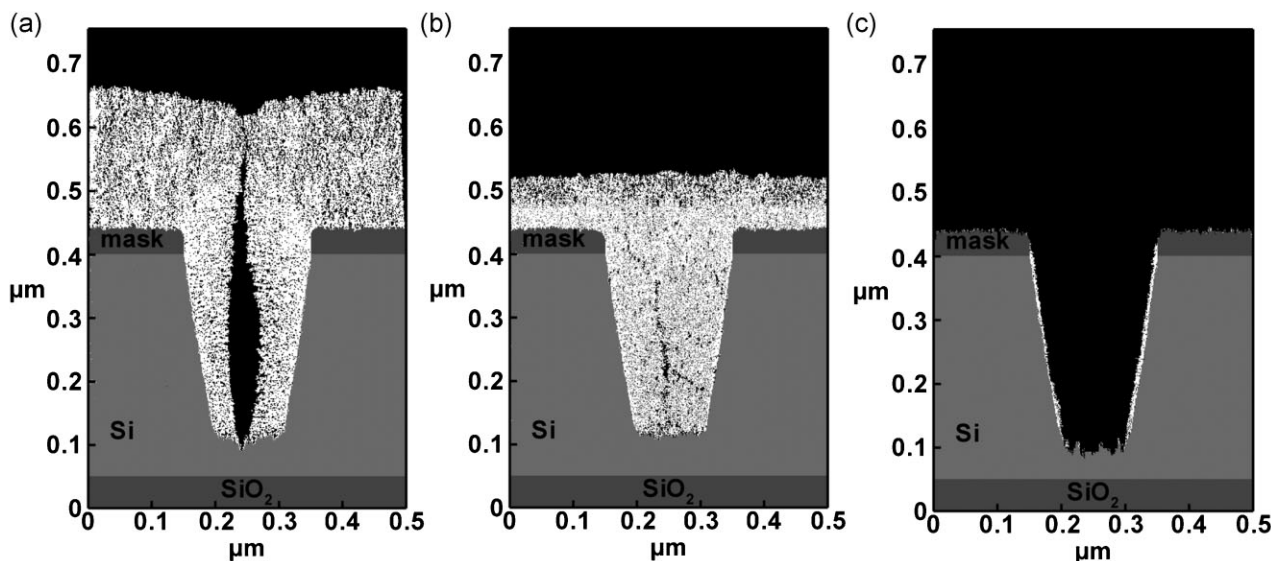

Figure 10. (a) Calculated deposition profiles at (a) 30% O_2, where a void is formed, (b) 54% O_2 where a proper gap filling process occurs, and (c) 70% O_2, where trench damage occurs.

© 2012 WILEY-VCH Verlag GmbH & Co. KGaA, Weinheim

It should be noted that this is, again, the chemical composition of the top surface layer which should have a lower oxygen content than the bulk of the deposited layer due to preferential sputtering of oxygen from the surface (see above). For this reason, the fraction of clean Si on the surface is relatively high (23%) at low oxygen content. At the lowest investigated O_2 gas fraction of 20% (and consequently a SiH_4 fraction of 64%), the deposited layer has a chemical composition of $SiH_{0,49}O_{0,75}$ which is indeed Si-rich. However at high O_2 gas fraction (90%), the composition is $SiH_{0,12}O_{1,40}$. As mentioned before, the bulk deposited layer contains even more oxygen, being close to SiO_2 with a negligible amount of hydrogen.

4. Conclusion

We have numerically investigated $Ar/SiH_4/O_2$ ICP used for the filling of Si trenches with SiO_2 by means of PECVD, as applied in STI. For this, a reaction set for plasma chemistry as well as for surface chemistry was created for $Ar/SiH_4/O_2$ ICPs on a poly-Si surface and presented here. The gas fractions of all three components were varied and the influence on the plasma characteristics and on the gap filling process was discussed. It was found that the most important species that account for deposition are SiH_2, SiH_3O, SiH_3, and SiH_2O while the most important ions that account for sputtering of the layer are SiH_3^+, SiH_2^+, O_2^+ and Ar^+.

The Ar gas fraction was varied while the SiH_4/O_2 ratio was kept fixed at 1:2. It was found that the deposition process is strongly influenced by the ratio of deposition *versus* sputtering. By varying the Ar fraction, this ratio can be tuned until a desired deposition rate is achieved. If the Ar fraction is too low ($<$16%), the deposition rate is dominant over sputtering, creating an undesired void when the trench is filled. At an Ar fraction above 60%, the deposition rate is too slow, resulting in damaging of the bottom of the trench and of the mask by sputtering. From the results it can be concluded that a gas mixture of 16% Ar, 30% SiH_4 and 54% O_2 results in a proper trench filling process.

It was found that oxidized Si-containing plasma species (SiH_3O, SiH_2O, SiHO, SiO and SiO_2) did not constitute the largest part of the plasma composition, indicating that rather low-volatile silane species (mainly SiH_3, SiH_2) are deposited and subsequently become oxidized, instead of being directly oxidized in the plasma before they deposit on the walls.

The SiH_4/O_2 ratio was varied while the Ar fraction was kept constant at 16%, and it was found that both the deposition rate and the chemical composition of the deposited layer were influenced. At the lowest investigated O_2 fraction of 20%, which yields a SiH_4/O_2 ratio of 3.2:1, the chemical composition of the top surface of the deposited layer was calculated as $SiH_{0,49}O_{0,75}$ which is considered Si-rich due to preferential sputtering of oxygen. The bulk of the deposited layer has a higher oxygen fraction, yielding a composition close to SiO_2, even at a low oxygen gas fraction of 20%, as could be concluded from the trench profile results where the bulk deposited layer was calculated.

Acknowledgements: S. Tinck is indebted to the Institute for the Promotion of Innovation by Science and Technology in Flanders (IWT Flanders). M. Kushner is acknowledged for providing the code and useful advice. M. Schaekers from IMEC is acknowledged for experimental support. Also, the CalcUA computing facilities of the University of Antwerp are acknowledged.

Received: May 14, 2011; Revised: December 23, 2011; Accepted: January 5, 2012; DOI: 10.1002/ppap.201100093

Keywords: argon; inductively coupled plasma (ICP); modeling; oxygen; plasma enhanced chemical vapor deposition (PECVD); silane

[1] Y. Chen, H. Yuan, Z. Zhang, N. Li, D. Chan, J. Chen, X. Li, G. Zhao, *ECS Trans.* **2010**, *27*, 679.
[2] H. Nishimura, S. Takagi, M. Fujino, N. Nishi, *Jpn. J. Appl. Phys.* **2002**, *41*, 2886.
[3] A. Boogaard, A. Y. Kovalgin, I. Brunets, A. A. I. Aarnink, J. Holleman, R. A. M. Wolters, J. Schmitz, *Surf. Coat. Technol.* **2007**, *201*, 8976.
[4] Y. Park, S. Rhee, *Surf. Coat. Technol.* **2004**, *179*, 229.
[5] A. Y. Kovalgin, A. Boogaard, I. Brunets, J. Holleman, J. Schmitz, *Surf. Coat. Technol.* **2007**, *201*, 8849.
[6] M. J. Kushner, *J. Appl. Phys.* **1988**, *63*, 2532.
[7] M. J. Kushner, *J. Appl. Phys.* **1993**, *74*, 6538.
[8] K. De Bleecker, D. Herrebout, A. Bogaerts, R. Gijbels, P. Descamps, *J. Phys. D: Appl. Phys.* **2003**, *36*, 1826.
[9] C. Y. Chang, J. P. McVittie, J. Li, K. C. Saraswat, *IEDM* **1993**, *93*, 853.
[10] Z. Hsiau, E. C. Kan, J. P. McVittie, R. W. Dutton, *IEEE Trans. Electron. Dev.* **1997**, *44*, 1375.
[11] M. J. Kushner, *J. Phys. D: Appl. Phys.* **2009**, *42*, 194013.
[12] R. J. Hoekstra, M. J. Grapperhaus, M. J. Kushner, *J. Vac. Sci. Technol. A* **1997**, *15*, 1913.
[13] I. G. Kouznetsov, A. J. Lichtenberg, M. A. Lieberman, *Plasma Sources Sci. Technol.* **1996**, *5*, 662.
[14] I. A. Kossyi, A. Y. Kostinsky, A. A. Matveyev, V. P. Silakov, *Plasma Sources Sci. Technol.* **1992**, *1*, 207.
[15] E. G. Thorsteinsson, J. T. Gudmundsson, *Plasma Sources Sci. Technol.* **2010**, *19*, 055008.
[16] S. Tinck, W. Boullart, A. Bogaerts, *J. Phys. D: Appl. Phys.* **2009**, *42*, 095204.
[17] C. Hsu, M. A. Nierode, J. W. Coburn, D. B. Graves, *J. Phys. D: Appl. Phys.* **2006**, *39*, 3272.
[18] S. Panda, D. J. Economou, M. Meyyappan, *J. Appl. Phys.* **2000**, *87*, 8323.

© 2012 WILEY-VCH Verlag GmbH & Co. KGaA, Weinheim

[19] B. Eliasson, M. Hirth, U. Kogelschatz, *J. Phys. D: Appl. Phys.* **1987**, *20*, 1421.
[20] T. J. Sommerer, M. J. Kushner, *J. Appl. Phys.* **1992**, *71*, 1654.
[21] S. J. B. Corrigan, *J. Chem. Phys.* **1965**, *43*, 4381.
[22] M. Hayashi, *J. Phys. (Paris)* **1979**, *40*, 45.
[23] C. F. Chan, "Reaction cross-sections and rate coefficients related to the production of positive ions", Lawrence Berkeley Lab. Report No. LBID-632, 1983.
[24] P. Banks, *Planet. Sp. Sci.* **1966**, *14*, 1085.
[25] A. Bogaerts, R. Gijbels, *Spectrochim. Acta B* **2002**, *57*, 1071.
[26] W. M. M. Kessels, K. Nadir, M. C. M. Van De Sanden, *J. Appl. Phys.* **2006**, *99*, 076110.
[27] R. Atkinson, D. L. Baulch, R. A. Cox, J. N. Crowley, R. F. Hampson, R. G. Hynes, M. E. Jenkin, M. J. Rossi, J. Troe, *Atmos. Chem. Phys.* **2004**, *4*, 1461.
[28] K. N. Joshipura, B. G. Vaishnav, S. Gangopadhyay, *Int. J. Mass. Spec.* **2007**, *261*, 146.
[29] S. Ramalingam, D. Maroudas, E. S. Aydil, S. P. Walch, *Surf. Sci.* **1998**, *418*, L8.
[30] S. P. Walch, S. Ramalingam, S. Sriraman, E. S. Aydil, D. Maroudas, *Chem. Phys. Lett.* **2001**, *344*, 249.
[31] E. Amantides, S. Stamou, D. Mataras, *J. Appl. Phys.* **2001**, *90*, 5786.
[32] S. Sriraman, E. S. Aydil, D. Maroudas, *J. Appl. Phys.* **2004**, *95*, 1792.
[33] S. Agarwal, M. S. Valipa, B. Hoex, M. C. M. Van De Sanden, D. Maroudas, E. S. Aydil, *Surf. Sci.* **2005**, *598*, 35.
[34] S. A. Vitale, B. A. Smith, *J. Vac. Sci. Technol. B* **2003**, *21*, 2205.
[35] M. A. Albao, D. J. Liu, C. H. Choi, M. S. Gordon, J. W. Evans, *Surf. Sci.* **2004**, *555*, 51.
[36] D. V. Daineka, F. Pradère, M. Châtelet, *Surf. Sci.* **2002**, *519*, 64.
[37] S. Hildebrandt, A. Kraus, R. Kulla, H. Neddermeyer, *Appl. Surf. Sci.* **1999**, *141*, 294.
[38] E. P. Gusev, H. C. Lu, T. Gustafsson, E. Garfunkel, *Appl. Surf. Sci.* **1996**, *104-105*, 329.
[39] H. Z. Massoud, *Microelectron. Eng.* **1995**, *28*, 109.
[40] S. Sriraman, M. S. Valipa, E. S. Aydil, D. Maroudas, *J. Appl. Phys.* **2006**, *100*, 053514.
[41] S. Agarwal, S. Sriraman, A. Takano, M. C. M. Van De Sanden, E. S. Aydil, D. Maroudas, *Surf. Sci. Lett.* **2002**, *515*, L469.
[42] S. Sriraman, S. Agarwal, E. S. Aydil, D. Maroudas, *Nature* **2002**, *418*, 62.
[43] N. Matsunami, Y. Yamamura, Y. Itikawa, N. Itoh, Y. Kazumata, S. Miyagawa, K. Morita, R. Shimizu, H. Tawara, *Atmos. Data Nucl. Data Tables* **1984**, *31*, 1.
[44] V. S. Smentkowski, *Prog. Surf. Sci.* **2000**, *64*, 1.
[45] D. H. Kim, G. H. Lee, S. Y. Lee, D. H. Kim, *J. Cryst. Growth* **2006**, *286*, 71.
[46] E. Collart, R. J. Visser, *Surf. Sci. Lett.* **1989**, *218*, L497.
[47] B. Lang, *Appl. Surf. Sci.* **1989**, *37*, 63.
[48] T. Mizutani, *J. Non-Cryst. Solids* **1995**, *181*, 123.
[49] M. P. Seah, T. S. Nunney, *J. Phys. D: Appl. Phys.* **2010**, *43*, 253001.
[50] M. Schaekers, IMEC *private communication*.

© 2012 WILEY-VCH Verlag GmbH & Co. KGaA, Weinheim